Closed-form representations of field components of fluorescent emitters in layered media

Mehmet Dogan,[1] M. Irsadi Aksun,[2] Anna K. Swan,[1,3] Bennett B. Goldberg,[1,3] and M. Selim Ünlü[1,3,*]

[1]*Physics Department, Boston University, 590 Commonwealth Avenue, Boston, Massachusetts 02215, USA*
[2]*Department of Electrical and Electronics Engineering, Koç University, Rumelifeneri Yolu 34450, Sarıyer Istanbul, Turkey*
[3]*Electrical and Computer Engineering Department, Boston University, 8 Saint Mary's Street, Boston, Massachusetts 02215, USA*
**Corresponding author: selim@bu.edu*

Received October 21, 2008; revised April 11, 2009; accepted April 13, 2009; posted April 29, 2009 (Doc. ID 103031); published May 27, 2009

Dipole radiation in and near planar stratified dielectric media is studied theoretically within the context of fluorescence microscopy, as fluorescent emitters are generally modeled by electric dipoles. Although the main emphasis of this study is placed on the closed-form representations of the field components of fluorescent emitters in layered environments in near- and far-field regions, the underlying motive is to understand the limits of spectral self-interference fluorescence microscopy in studying the dipole orientation of fluorophores. Since accurate calculations of the field components of arbitrarily polarized electric dipoles in layered environments are computationally very time-consuming, a method for finding their closed-form representations is proposed using the closed-form potential Green's functions previously developed for microwave applications. The method is verified on typical geometries used in spectral self-interference microscopy experiments, where a dipole emitter is positioned over a slab of SiO_2 on top of a Si substrate. In addition to facilitating efficient calculation of near and intermediate fields of fluorescent emitters, closed-form Green's functions for fields would also play a crucial role in developing efficient and rigorous computational analysis and design tools for optical passive devices such as optical antennas by significantly improving the computational cost of the numerical solution of the integral equation. © 2009 Optical Society of America

OCIS codes: 260.2510, 260.2110, 260.3160, 350.5500, 350.5610.

1. INTRODUCTION

For more than a century, it has been known that fluorescence emission is modified by the presence of dielectric and metal surfaces near fluorescent emitters [1]. Drexhage studied fluorescence emission and lifetime near metal and dielectric surfaces [2]. Later, modified fluorescent emission was utilized, which led to the development of a technique called fluorescence light intensity contrast microscopy (FLIC), which determines the position of fluorescent dyes with respect to reflecting surfaces by analyzing the intensity of the fluorescence signal [3]. This technique enabled the study of various biological structures and processes on oxidized silicon substrates, such as cell adhesion [4,5], cellular membranes [6], and molecular motors [7]. A similar technique, spectral self-interference fluorescence microscopy (SSFM), which uses spectral modifications of the fluorescence emission, has also been introduced for subnanometer position determination of fluorescent emitters above dielectric surfaces [8]. Using the SSFM technique in the far field, DNA conformation on surfaces was studied [9].

In all of the applications mentioned, in order to draw conclusions from the fluorescence measurements, it is crucial to model the fluorescence signal detected at a certain observation point for a given position of the emitter in a given material system and geometry. A comprehensive electromagnetic model for SSFM has previously been introduced with the far-field approximations since fluorescence emission is detected at distances much larger than the wavelength of the radiation from the dipoles [10]. However, since the definitions of near- and far-field zones for radiators in or near layered media are not as clear as those of a free-standing radiator in free space, having a computational tool that could provide the fields, and in turn power density and intensity, accurately and efficiently would eliminate any uncertainties about the resulting intensity distributions from SSFM. In addition, such an accurate and efficient calculation of the fields and radiation intensity may provide additional information about the radiator and its environment, such as the polarization of the emitter and the layer profile.

In this paper, the discussion is extended to developing a robust and comprehensive yet efficient algorithm for the calculation of closed-form electric and magnetic fields not only in the far field but also in the near and intermediate fields of radiating dipoles near dielectric stratified media. Initially, in Section 2, the formulation of the dipole radiation problem is introduced for a general planar stratified dielectric medium, and closed-form electric and magnetic field Green's functions are given in terms of vector and scalar potential Green's functions. Then, in Section 3, an efficient method of finding potential Green's functions is summarized, and in Section 4 electric and magnetic field Green's functions are found in terms of complex image

 © 2009 Optical Society of America

terms. Finally, in Section 5, several field and intensity calculation examples are given for typical SSFM substrate geometries, and dipole polarization determination is discussed.

2. FORMULATION OF THE PROBLEM

Radiation from infinitesimal dipoles, horizontal and vertical with respect to the layer interface, has attracted a great deal of interest for a long time, starting in early 1900s [11]. This interest was initially directed toward understanding the physical mechanisms of the wave constituents of electromagnetic wave propagation in layered structures [12,13] and then to rigorous analysis of electromagnetic waves in microwave circuits, antennas, and optics [14–22]. However, as stated above, the main goals of this work are (1) to derive accurate closed-form expressions for the fields of dipoles in layered media that are valid not only in the far-field but also in the near- and intermediate-field regions, (2) to facilitate an efficient and accurate modeling of fluorescent emitters in layered environments, and (3) to provide a computational tool for the analysis of optical circuits.

Fluorescence is a spontaneous process, and thus fluorescence emission from fluorescent emitters within an excitation volume is incoherent. So, in determining the total fluorescence intensity, the contribution from each emitter should be integrated incoherently; that is, the integration should be performed at the intensity level rather than at the field amplitude level. However, even so, the calculations should be done at the single molecule level. That is why, in the study of materials with the use of fluorescence microscopy, the radiation from excited fluorophores, each of which is modeled as an electrical dipole, is of primary interest. Since the emitters are several orders of magnitude smaller than the wavelength of the radiation, they can be considered to be point sources, and Green's function formalism can be used, because the Green's function is the solution to inhomogeneous differential equations where the source term is a delta function.

Before concentrating on the specific material systems, it would be instructive to formulate the problem in a more general setting: a planar multilayered dielectric medium with a dipole, as shown in Fig. 1. The dipole is positioned in layer i and is represented by an associated current distribution vector, **J**. The electromagnetic properties of the isotropic layers, namely, magnetic permeability μ and electric permittivity ε, vary in one direction only; that is, the direction of stratification is assumed to be the z direction, and the geometry has a cylindrical symmetry. In this general setting, the vector potential Green's function can be represented by a dyad defined as

$$\bar{\bar{\mathbf{G}}}^{\mathbf{A}} = \hat{x}\hat{x}G^A_{xx} + \hat{y}\hat{y}G^A_{yy} + \hat{z}\hat{z}G^A_{zz} + \hat{z}\hat{x}G^A_{zx} + \hat{z}\hat{y}G^A_{zy}, \tag{1}$$

with the associated scalar potential Green's functions due to the horizontal and vertical components of the dipole, G^Q_h and G^Q_z, respectively. The first subscripts in the vector potentials show the polarization of the observed field, and the second subscripts denote the direction of the dipole source.

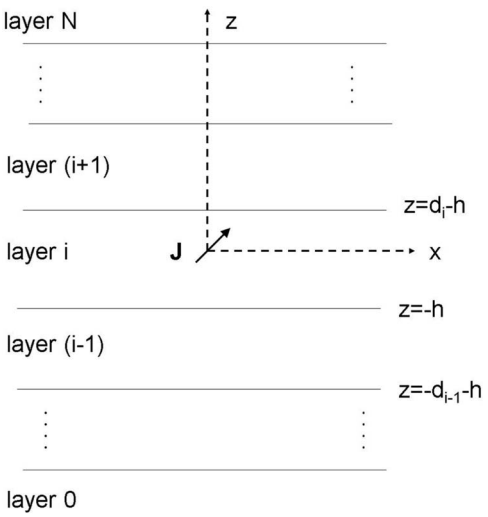

Fig. 1. Radiating dipole in planarly layered media.

For the sake of clarifying the notation used throughout, the current density **J** is written as $\mathbf{J}=\hat{\alpha}Il\,\delta(r)$ due to a point dipole source with arbitrary orientation $\hat{\alpha}$ and the current moment Il, which is assumed to be unity without loss of generality. The linearity of Maxwell's equations and the medium allows one to decompose the electric dipole into two orthogonal components: a vertical electric dipole (VED), $\hat{\alpha}=\hat{z}$, and a horizontal electric dipole (HED), $\hat{\alpha}\perp\hat{z}$. Since the planar geometry stratified in the z direction is cylindrically symmetric around the z axis, the direction of the HED can be assumed to be along the x axis, again with no loss of generality. Therefore, any field component due to such a dipole source can be obtained from the three components of the vector potential Green's functions, G^A_{xx}, G^A_{zx}, G^A_{zz}, and the two scalar potential Green's functions, G^Q_x and G^Q_z, which are due to the horizontal and vertical components of the dipole, respectively. Once the Green's functions of scalar and vector potentials are defined in layered media, the Green's functions for the field components can be expressed in terms of those of the potentials, as given below for the field components due to an HED as an example.

Electric field components for an HED:

$$G^E_{xx} = -j\omega\left(G^A_{xx} + \frac{1}{\omega^2}\frac{\partial^2}{\partial x^2}G^Q_x\right), \tag{2a}$$

$$G^E_{yx} = \frac{1}{j\omega}\frac{\partial^2}{\partial y\,\partial x}G^Q_x, \tag{2b}$$

$$G^E_{zx} = -j\omega\left(G^A_{zx} + \frac{1}{\omega^2}\frac{\partial^2}{\partial z\,\partial x}G^Q_x\right). \tag{2c}$$

Magnetic field components for an HED:

$$G^H_{xx} = \frac{1}{\mu}\left(\frac{\partial G^A_{zx}}{\partial y}\right), \tag{3a}$$

$$G^H_{yx} = \frac{1}{\mu}\left(\frac{\partial G^A_{xx}}{\partial z} - \frac{\partial G^A_{zx}}{\partial x}\right), \tag{3b}$$

$$G_{zx}^{H} = \frac{1}{\mu}\left(-\frac{\partial G_{xx}^{A}}{\partial y}\right), \tag{3c}$$

where the projection of the dipole on the plane of the layers ($x-y$ plane) has been set arbitrarily to the x direction. Once the Green's functions of the potentials are written in closed forms as the explicit functions of the space coordinates, the field Green's functions can also be obtained in closed forms just by analytical differentiations, as seen from Eqs. (2) and (3). Therefore, it would be instructive to review briefly the method of obtaining the closed-form Green's functions of potentials via the discrete complex image method (DCIM).

3. CLOSED-FORM GREEN'S FUNCTIONS OF POTENTIALS IN THE SPACE DOMAIN

In the previous section, fields are expressed in terms of potentials for a general stratified geometry. In this section, the method of getting the vector potential and scalar potential Green's functions, as well as some key issues, will be briefly discussed, with a view of employing the method in self-interference fluorescence microscopy. Although the method is applicable for any number of layers with any type of material, the discussion here is presented for a three-layer medium commonly employed in the experimental setup of self-interference microscopy: fluorophore (modeled as an electric dipole in this study) on top of SiO_2/Si substrate, i.e., a thin SiO_2 slab sandwiched between free space and a thick Si layer. For the sake of presentation of the formulation, the source is assumed to be an HED and located, together with the observation points, in the top semi-infinite free space, denoted by layer i in the following discussions. Note that the Green's functions for a VED can also be obtained by following the same arguments to be discussed.

The method for finding the scalar and vector potential Green's functions can be outlined as follows:

(1) Spectral-domain Green's functions in the observation layer are obtained analytically.
(2) Spectral-domain Green's functions are approximated in terms of exponentials.
(3) Spatial-domain Green's functions are obtained in closed forms by taking the inverse Hankel transforms of their spectral-domain counterparts analytically, with the use of the Sommerfeld identity.

Since some of the work related to these steps has already been presented in detail elsewhere at microwave frequencies [23–25], for the sake of brevity, the steps are not going to be repeated here unless some modifications become necessary due to the application of the approach at higher frequencies, namely, at optical frequencies. As is stated in the first step, the Green's functions of the vector and scalar potentials in the spectral domain can be obtained in closed forms analytically, and their derivations and steps have been detailed in [24]. Therefore, using the expressions from the reference, two relevant Green's functions necessary for the x component of the electric field due to an HED are tailored for the geometry and given as

$$\tilde{G}_{xx}^{A} = \frac{\mu_i}{j2k_{zi}}[e^{-jk_{zi}|z|} + \tilde{R}_{TE}^{i,i-1}e^{-jk_{zi}(z+2h)}], \tag{4a}$$

$$\tilde{G}_{x}^{Q} = \frac{1}{j2k_{zi}\epsilon_i}\left[e^{-jk_{zi}|z|} + \frac{k_i^2\tilde{R}_{TE}^{i,i-1} + k_{zi}^2\tilde{R}_{TM}^{i,i-1}}{k_\rho^2}e^{-jk_{zi}(z+2h)}\right]. \tag{4b}$$

where the tilde over Green's functions denotes the spectral-domain representation, tilde over the reflection coefficients denotes the generalized reflection coefficients, which account for the multiple reflections from all interfaces in the geometry, and k_{zi} is the wavenumber in the axial direction for the ith layer. In the above expressions, the first terms in the square brackets represent the direct waves from the source point to the observation point, while the second terms represent the reflected waves at the observation plane due to the incident waves impinging upon the interface between the semi-infinite free space and the slab. Since the spatial-domain Green's functions are defined as the inverse Hankel transforms of their spectral-domain counterparts, Eqs. (4a) and (4b) need to be transformed either numerically or analytically if possible. However, it is a well-known fact that the spectral-domain Green's functions of potentials and fields cannot be analytically transformed in general, except for a rather trivial geometry of homogenous unbounded medium, and that their numerical transformations are extremely time-consuming due to the oscillatory and slow-decaying nature of the integrands. The whole idea of getting the closed-form Green's functions in the spatial domain is based on the Sommerfeld integral identity,

$$\frac{e^{-jk_i r}}{r} = \frac{-j}{2}\int_{SIP} \mathrm{d}k_\rho k_\rho H_0^{(2)}(k_\rho\rho)\frac{e^{-jk_{zi}|z|}}{k_{zi}}, \tag{5}$$

which provides a pair of Hankel transformable functions in closed forms. Using this information together with the generic form of the spectral-domain Green's functions as given in Eq. (4), it would be sufficient to approximate the reflected wave terms in the spectral-domain expressions of the Green's functions in terms of complex exponentials [23–25]. As a result of this procedure, the reflected waves in the spectral domain are approximated as the sum of spherical waves with complex distances r in the spatial domain, because the Sommerfeld identity in Eq. (7) can result only in spherical waves. Because of this, the method is commonly referred to as the DCIM, and cannot properly approximate other wave natures, such as cylindrical and conical waves, also known as surface and lateral waves, respectively, if not properly handled [26]. However, since both the source and observation planes are away from the major reflecting surface for the self-interference experiment, the surface and lateral waves would have negligible contributions at the observation plane. Having briefly introduced the procedure and the underlying idea of the method, we now discuss its implementation and critical issues with a view to extending the method to optical frequencies and to field components.

In the implementation of the DCIM for the analytic evaluation of the inverse Hankel transformation of Eqs. (4a) and (4b), there are two important steps that would have significant effects on the accuracy and robustness of

the method: the choices of (i) the sampling path and (ii) the exponential approximation method. The former is rather important for the cases where the surface waves and lateral waves are significant contributors of the fields; otherwise the path proposed in the two-level algorithm would be quite satisfactory [25]. For the exponential approximation, the generalized pencil-of-function method has been used because of its robustness and less noise sensitivity [27] in comparison with other methods, such as various versions of Prony's method. Based on these choices of the sampling path and the exponential approximation method, the second terms in the square brackets, excluding the exponential parts, in Eq. (4) are sampled and approximated by complex exponentials, resulting in explicit functions of the source and observation points, h and z, respectively, in addition to the lateral distance, ρ. Note that having the source and observation points explicit in the closed-form expressions is important for this application in order to be able to cast the Green's functions of the fields in closed forms, as they are obtained by the spatial differentiations of the Green's functions of the potentials; see Eqs. (2) and (3). Moreover, this form of the Green's functions would also be advantageous in inverse problems, since the main goal in fluorescence experiments, where the fluorophore is located in the vicinity of dielectric materials, is to determine the axial location and the orientation of the dipole.

As a result of the outlined procedure, the spectral-domain Green's functions for the potentials are obtained as

$$\tilde{G}_{xx}^{A} = \frac{\mu_i}{j2k_{zi}}\left[e^{-jk_{zi}|z|} + \sum_{n=1}^{N_1} a_{1n}\, e^{-jk_{zi}(z+2h-j\alpha_{1n})} + \sum_{n=1}^{N_2} a_{2n}\, e^{-jk_{zi}(z+2h-j\alpha_{2n})}\right], \tag{6a}$$

$$\tilde{G}_{x}^{Q} = \frac{1}{j2k_{zi}\epsilon_i}\left[e^{-jk_{zi}|z|} + \sum_{n=1}^{N_3} b_{1n}\, e^{-jk_{zi}(z+2h-j\beta_{1n})} + \sum_{n=1}^{N_4} b_{2n}\, e^{-jk_{zi}(z+2h-j\beta_{2n})}\right], \tag{6b}$$

where the two sums in the approximations are due to the two-level approach [25]. Hence, with the help of the Sommerfeld identity (5), the corresponding spatial-domain Green's functions are simply written as

$$G_{xx}^{A} = \frac{\mu_i}{4\pi}\left[\frac{e^{-jk_i r}}{r} + \sum_{n=1}^{N_1+N_2} a_n \frac{e^{-jk_i r_{\alpha n}}}{r_{\alpha n}}\right], \tag{7a}$$

$$G_{x}^{Q} = \frac{1}{4\pi\epsilon_i}\left[\frac{e^{-jk_i r}}{r} + \sum_{n=1}^{N_3+N_4} b_n \frac{e^{-jk_i r_{\beta n}}}{r_{\beta n}}\right], \tag{7b}$$

where the distances between the source (real or images) and the observation points r, $r_{\alpha n}$, and $r_{\beta n}$ are expressed in terms of the axial coordinate z and the lateral coordinate ρ, as $r=[\rho^2+z^2]^{1/2}$ for the direct term and as $r_{\gamma n}=[\rho^2+(z+2h-j\gamma_n)^2]^{1/2}$, $\gamma=\alpha,\beta$, for the complex images.

4. ANALYTICAL DERIVATION OF ELECTRIC AND MAGNETIC FIELD GREEN'S FUNCTIONS

Analytical expressions relating the field Green's functions to the potential Green's functions and also the closed-form expressions of the potential Green's functions have been derived and presented in Eqs. (2) and (3) and Eq. (7), respectively. Since the former involves spatial derivatives and the latter involves explicit functions of z and ρ, it would be a simple matter to get the field Green's functions in closed forms, as the magnetic field Green's functions contain only the first-order spatial derivatives of the vector potentials, and the electric field Green's functions contain the vector potentials and the second-order derivatives of the scalar potentials. For the sake of completeness, a few steps of this derivation and one of the resulting field Green's functions are provided in this section.

In order to facilitate the differentiations of spherical waves in the approximations of the potential Green's functions (7), it would be instructive to state the forms of the three types of the derivatives involved in the expressions:

$$\text{(i)}\ \partial/\partial x, \partial/\partial y, \partial/\partial z,$$

$$\text{(ii)}\ \partial^2/\partial x^2, \partial^2/\partial y^2, \partial^2/\partial z^2,$$

$$\text{(iii)}\ \partial^2/\partial x\partial y, \partial^2/\partial x\partial z, \partial^2/\partial y\partial z.$$

So the first-order derivatives of the spherical waves with complex distances r_c are simply written as

$$\frac{\partial}{\partial\eta}\left(\frac{e^{-jkr_c}}{r_c}\right) = -\frac{e^{-jkr_c}}{r_c}\left(\frac{(jkr_c+1)\eta}{r_c^{\,2}}\right), \tag{8a}$$

where η could be any of x, y, or z. By using the results of the first-order derivatives, the second order derivatives on the same variables and on the two different variables are obtained as

$$\frac{\partial^2}{\partial\eta^2}\left(\frac{e^{-jkr_c}}{r_c}\right) = \frac{e^{-jkr_c}}{r_c}\left(-\frac{jk}{r_c} - \frac{(1+k^2\eta^2)}{r_c^{\,2}} + \frac{j3k\eta^2}{r_c^{\,3}} + \frac{3\eta^2}{r_c^{\,4}}\right), \tag{8b}$$

$$\frac{\partial^2}{\partial\eta\partial\zeta}\left(\frac{e^{-jkr_c}}{r_c}\right) = \frac{e^{-jkr_c}}{r_c}\frac{\eta\zeta}{r_c^{\,2}}\left(-k^2 + j3k\frac{1}{r_c} + \frac{3}{r_c^{\,2}}\right), \tag{8c}$$

respectively, where two distinct variables η and ζ could be replaced by any two of x, y and z. Note that the complex nature of the distance r_c is due mainly to a complex shift in the z variable as in the cases of $r_{\alpha n}$ and $r_{\beta n}$; as a result, when the z derivative is performed for the dummy variables, η and/or ζ, the corresponding variable(s) in Eqs. (8a)–(8c) need to be replaced by z, $z+2h-j\alpha_n$, or $z+2h-j\beta_n$, depending on the form of $r_c=r$, $r_{\alpha n}$, or $r_{\beta n}$, respectively. As an example, the explicit form of the x component of the electric field Green's function due to the x directed electric dipole is given as

$$G_{xx}^{E} = -j\omega\left\{\frac{\mu_i}{4\pi}\left[\frac{e^{-jk_i r}}{r} + \sum_{n=1}^{n=N_1+N_2} a_n \frac{e^{-jk_i r_{\alpha n}}}{r_{\alpha n}}\right] + \frac{1}{\omega^2}\frac{1}{4\pi\epsilon_i}\left[\frac{e^{-jk_i r}}{r}\left(-\frac{jk_i}{r} - \frac{(1+k_i^2x^2)}{r^2} + \frac{j3k_ix^2}{r^3} + \frac{3x^2}{r^4}\right) + \sum_{n=1}^{n=N_3+N_4} b_n \frac{e^{-jk_i r_{\beta n}}}{r_{\beta n}}\left(-\frac{jk_i}{r_{\beta n}} - \frac{(1+k_i^2x^2)}{r_{\beta n}^2} + \frac{j3k_ix^2}{r_{\beta n}^3} + \frac{3x^2}{r_{\beta n}^4}\right)\right]\right\} \quad (9)$$

5. RESULTS AND DISCUSSION

The closed-form field expressions presented so far can be used as the starting point for any further calculations to determine the collection efficiency function (CEF) of a fluorescence-based optical system. The details of the treatment would depend on the specifics of the collection system. For example, in his work, Enderlein [28] considers a confocal pinhole and calculates the energy flux through the pinhole in a confocal system, while Vamivakas *et al.* [28] find the CEF by calculating the overlap integral of the focused field with the fiber mode where a fiber-based confocal microscopy system is considered.

In the next set of examples, typical SSFM geometries are considered, where a dipole emitter is placed 5 nm above a 5-μm-thick SiO_2 that is situated on top of a thick (semi-infinite) Si substrate. The refractive indices of Si and SiO_2 are determined by wavenumber-dependent polynomials valid in the 17,000–20,000 cm^{-1} spectral range. Si is absorptive in this range and is assumed to have a complex refractive index profile. The real part is given by $n_0(\tilde{\nu})=a+b\tilde{\nu}+c\tilde{\nu}^2+d\tilde{\nu}^3$, where $\tilde{\nu}$ represents the wavenumber. The coefficients are $a=2.946$, $b=1.157\times10^{-4}$ cm, $c=-7.961\times10^{-9}$ cm^2, and $d=2.773\times10^{-13}$ cm^3. The imaginary part is described by $k_0(\tilde{\nu})=e+f\tilde{\nu}+g\tilde{\nu}^2+h\tilde{\nu}^3$ with $e=-0.1354$, $f=3.149\times10^{-5}$ cm, $g=-2.506\times10^{-9}$ cm^2, and $h=7.172\times10^{-14}$ cm^3. The SiO_2 refractive index has only a real part given as $n_1(\tilde{\nu})=p+q\tilde{\nu}+r\tilde{\nu}^2$, where the coefficients are $p=1.445$, $q=4.151\times10^{-7}$ cm, and $r=2.370\times10^{-11}$ cm^2. The wavelength of the radiation was assumed to be 500 nm for monochromatic calculations, and corresponding refractive indices are determined from the polynomial forms. Green's functions are calculated for this material system by following the procedure described in the previous sections. A total of 26 complex images are used in determining each one of five potential Green's functions in terms of complex exponentials. Fifteen of the complex exponentials are determined by the first step of the two-level approach described in [25], and eleven of them are determined by the second step. Therefore, $N_1=N_3=15$ and $N_2=N_4=11$ in Eq. (6) and (7).

When the observation points are assumed to be at the front surface of a microscope objective, the axial distance from the objective to the dipole emitter is the working distance of the objective. For the 0.12 numerical aperture (NA), 5× magnification objective used in the previous SSFM experiments, the working distance is 14 mm. In Fig. 2, the normalized magnitude of the x components of the electric fields due to an HED, a dipole with 60 deg polar angle, and a VED are shown at the axial observation distance of $z=14$ mm along the x axis. The plots give the values of the electric fields for as large as $x=8$ mm, corresponding to an observation polar angle of about 30 deg to present the spatial variations due to the interference effects created by the interfaces. In the typical SSFM experiments, where the spectral variations are used for determining the axial position of emitters, small-NA objectives are preferred to minimize the signal collection to the first lobe. Limiting the NA to small values is crucial, because the spectral modulations are diminished if the spatially varying signal from larger angles is collected as well [30]. Both in the previous experiments and in the calculations [8,9], the maximum polar angle of the objective was chosen to be about 6.9 deg and the cutoff for the signal collection along the x axis then corresponds to 1.68 mm.

For large axial observation values, the electric fields calculated by introducing the far-field approximations overlap the values determined by the rigorous method explained in this work and thus are not plotted in Fig. 2. It was also shown in [31] that the far-field approximations are valid and sufficient when the fluorescence signal is collected in the far field of the emitters. Thus, in conventional microscopy systems utilizing an objective for light collection, the far-field approximation would suffice. However, far-field approximations start to fail for observation distances that are comparable to the physical size of the reflecting structures. In the substrates used for SSFM,

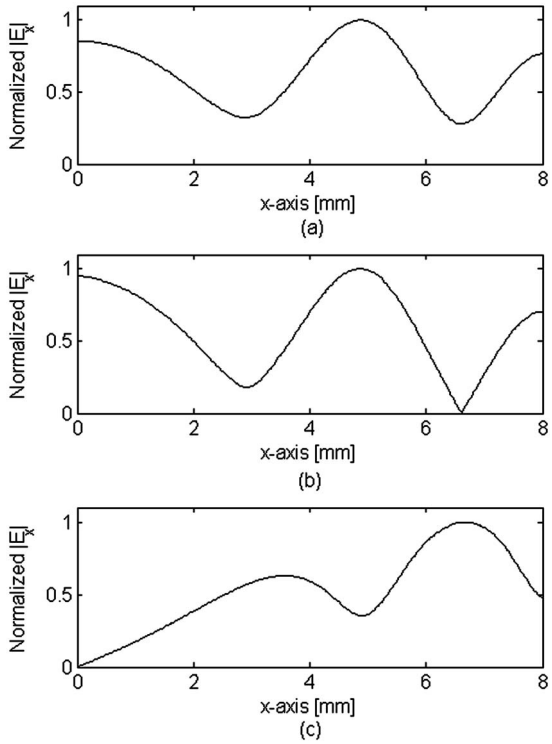

Fig. 2. Normalized magnitude of the x component of the electric fields along the x axis at an observation height of $z=14$ mm due to (a) HED, (b) dipole with a polar angle of 60 degrees, and (c) VED for 500 nm.

the nominal thickness of the SiO_2 layer is 5 μm, and at the distances above the top surface comparable to 5 μm, the field values cannot simply be calculated using far-field approximations. Such an experimental configuration would arise if an optical fiber is used for light collection in fluorescence spectroscopy. A typical fiber collection utilizing NA values compatible with SSFM would require placement of the fiber in the middle field to conserve collection efficiency. In Fig. 3, the rigorous results are compared with the results determined using far-field approximations for two dipole orientations: HED and VED. The field values are calculated at $z=5$ μm along the x axis. The plots show that for both dipole orientations, the far-field approximations do not properly explain the field distributions. While the far-field approximations show larger spatial variations, the rigorous calculations predict smaller depths in the spatial modulations correctly. The smaller depths are expected because as the observation point becomes closer to the source, the field distribution converges to the free-space radiation pattern, which is free of spatial modulations. Simply stated, the contributions from the direct radiation start dominating in comparison with the complex image contributions, namely, contributions from the reflections.

The intermediate region between the far field and the near field is referred to as middle-field region in the literature [32,33]. The rigorous method presented here could be a useful tool in the analysis of optical signals collected in the middle-field region since the far-field approximations fail to explain the radiation pattern in this intermediate regime.

In the optical experiments, the directly measured quantity is the optical power, rather than the fields themselves. The collected optical power is a function of the aperture size of the collection system and the projection of the Poynting vector on the aperture. In the most practical applications, the signal collecting objective lens (or optical fiber) is placed on top of the source with the objective's axis being parallel to the optical axis z. So only the axial component of the Poynting vector S_z over the objective clear aperture perpendicular to the optical axis would be sufficient to calculate the optical energy collected by the objective. Ultimately, the field components transverse to the optical axis, that is, E_x, E_y, H_x, and H_y, are required for determining S_z. In Fig. 4, the normalized axial component of the Poynting vector generated by a VED is presented as a function of transverse radial direction for several axial observation positions. The Poynting vector plots also show that when the signal is probed near the source, the direct radiation term dominates and the resulting signal profile resembles the free-space source [Fig. 4(a)]. Again, similar to the fields, the spatial oscillations in the Poynting vectors in the middle-field region start to appear [Figs. 4(b) and 4(c)]. In the far field, the contributions from the direct and the reflected waves are comparable and there are deeper spatial modulations of the optical signal.

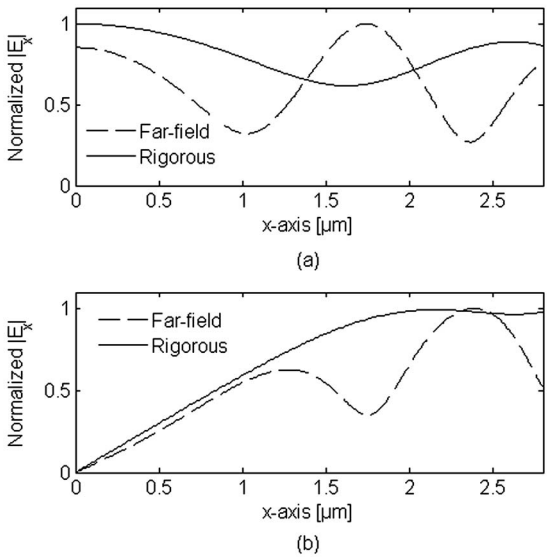

Fig. 3. Normalized magnitude of the x component of the electric fields due to (a) HED and (b) VED. Calculations are done for $z=5$ μm along the x axis for 500 nm. Solid curves, results for the rigorous calculations presented in this work; dashed curves, results for the far-field approximations.

The presence of reflecting dielectric interfaces in the vicinity of dipole sources introduces structures to the spatial radiation profiles, as can be seen in Figs. 2–4. Modification of the dipole radiation pattern depends on the properties and the physical size of the substrates, which can in turn be determined by measuring either the spatial or the spectral profile of the radiation. Furthermore, dipole radiation is directional and the radiation profile also depends on the orientation of the dipole. Similarly to finding the position of the emitters, one can find ways to determine the orientation of the emitters by exploiting the structured emission pattern. Several techniques have previously been introduced for orientation determination [34–36]. Utilizing spectral acquisition for determining orientation could be another approach since the structures in the emission pattern are scaled by wavelength. As long as the axial positions of the emitters are fixed and known, orientation of the dipole emitters can be estimated by analyzing the shifts in the spectral fringes in the collected emission spectrum. In the analysis, the rigorous method developed here could be useful.

As an example, two spectral responses are given in Fig. 5(a) for two orientations of a dipole emitter with polar angles of 10 deg and 60 deg. The maximum collection angle of the objective is assumed to be 19 deg, and the observation points are again 14 mm above the source, so the maximum radial distance for the collection is 4.8 mm at the collection plane. This radial limit corresponds to the peak of the first side lobe for HED and the minimum between the main lobe and the side lobe for VED as can be seen in Fig. 2. In the calculations, the axial component of the Poynting vector is integrated over the lens aperture to find the optical power for each wavelength component. The optical power calculations are repeated for each wavelength within the desired bandwidth to generate the spectral plots. The change in the spectral response is rather drastic for two orientations of the dipole, and the shifts in the spectral fringes are clearly visible when the spectral response of dipole emitters with polar angles of 10 deg and 60 deg are compared.

Quantifying the spectral shifts for various polar angle values is crucial to understand the effects of dipole polar-

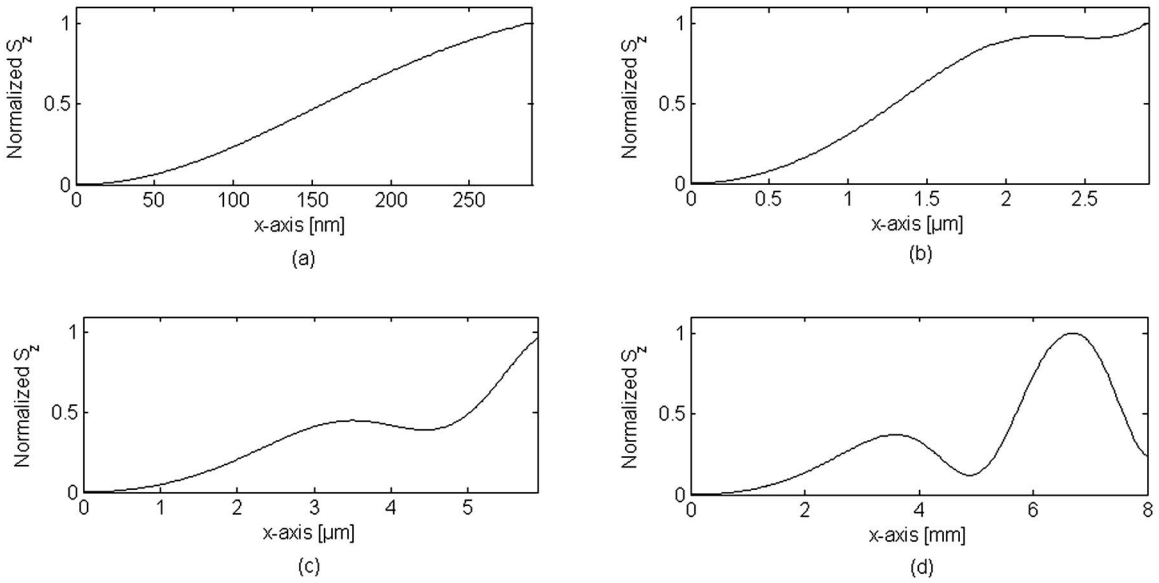

Fig. 4. Vertical component of the Poynting vector as a function of the x axis due to a VED for 500 nm. Axial components of the observation points are (a) 500 nm, (b) 5 μm, (c) 10 μm, (d) 14 mm. The transition from the smooth to a structured profile is observed as the detection points are moved away from the source.

ization on the spectral emission patterns. Figure 5(b) shows the differential spectral shift referenced to the VED spectrum, as a function of the polar angle of the dipole. Several polar angles are given for three maximum collection angle values of 15 deg (NA=0.26), 19 deg (NA =0.33), and 22 deg (NA=0.37). The spectral shifts reveal that the spectrum is more sensitive to the changes of dipole orientation for lower dipole polar angles, since the curves are steeper. As the dipole polar angle approaches to 90 deg (HED), the spectrum becomes less sensitive to the changes in dipole angles. The loss in the sensitivity starts to appear at about 20 deg for the objective collection angle of 15 deg. The plateau, after the onset, in the curves shifts to larger dipole angles as the objective collection angle increases: 30 deg dipole angle for 19 deg maximum collection angle of the objective and about 60 deg dipole angle for 22 deg collection angle. Depending on expected dipole angles, the objective collection angle can be adjusted to the optimum value. A set of measurements by varying the objective NA might also be advantageous in determining the dipole orientation. Optimization of the collection angles and development of aperture filters might further increase the sensitivity of the spectral shifts to the changes in the dipole orientation, and potentially SSFM could reveal the orientation of dipoles.

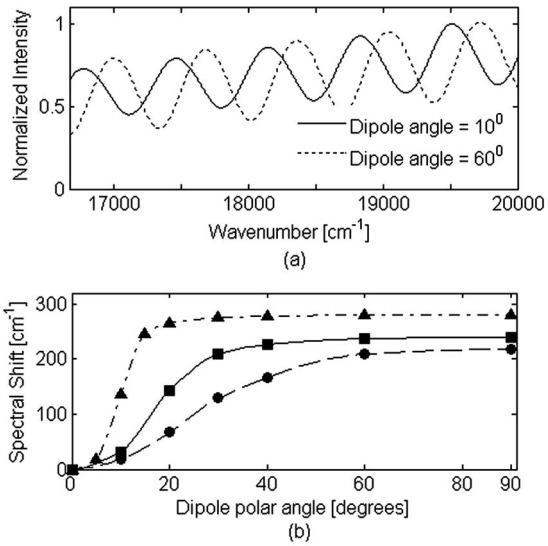

Fig. 5. (a) Spectral response of two dipoles oriented at a polar angle of 10 deg (solid curve) and 60 deg (dashed curve) as a function of the wavenumber of the dipole emission within in a bandwidth of 16,667–20,000 cm^{-1} (500–600 nm). The collection angle of the objective is assumed to be 19 deg. (NA=0.33). (b) Spectral shift of fringes in the emission spectrum of dipoles with various polar angles referenced to the spectral fringes due to a VED (polar angle=0 deg). The three curves are for objective collection angles of 15 deg (triangles), 19 deg (squares), and 22 deg (circles).

6. CONCLUSION

A method for finding closed-form electric and magnetic field Green's functions is presented for point dipole emitters in multilayered dielectric media using the closed-form potential Green's functions previously developed for microwave applications. With the method proposed in this work, it is possible to determine the fields produced by arbitrary-oriented electric dipoles in or near isotropic multilayered media in a computationally efficient and robust way due to the reduction of numerical calculations in finding the potential Green's functions. Far, near, and middle fields of radiating dipoles near dielectric interfaces can be calculated within the same scheme. Thus, the proposed method is useful both in verifying the validity of far-field approximations and providing tools for middle-field calculations where far-field approximations fail. In general, the approach demonstrated in this work can be

applied to electromagnetic systems, including optical microscopes in biological imaging, to find fluorescence intensity at desired detection points and can also be used to test the validity of the approximations. Closed-form Green's functions for fields not only facilitate efficient calculation of near and intermediate fields of fluorescent emitters but also play a crucial role in developing efficient and rigorous computational analysis and design tools for passive optical devices such as optical antennas. Since Maxwell's equations are linear equations if the involved media are linear, the governing equations of electromagnetic waves can be written in the form of integral equations with the Green's functions as their kernels. Hence, having a closed-form kernel rather than an integral over an infinite domain significantly improves the computational cost of the numerical solution of the integral equation.

ACKNOWLEDGMENTS

This work was supported in part by the U.S. National Science Foundation (NSF) under grant DBI 0138425 and award EEC-9987821 of the Engineering Research Centers Program; in part by the U.S. Air Force Office of Scientific Research (AFOSR) under grant MURI F-49620-03-1-0379; in part by the National Institutes of Health (NIH), National Institute of Biomedical Imaging and Bio Engineering, under grant 5R01 EB00 756-03; and in part by The Scientific and Technological Research Council of Turkey (TUBITAK) under grant 106E068.

REFERENCES

1. O. Wiener, "Stehende Lichtwellen und die Schwingungrichtung polarisirten Lichtes," Ann. Phys. Chem. **40**, 203–243 (1890).
2. K. H. Drexhage, "Interaction of light with monomolecular dye layers," Prog. Opt. **12**, 163–232 (1974).
3. A. Lambacher and P. Fromherz, "Fluorescence interference-contrast microscopy on oxidized silicon using a monomolecular dye layer," Appl. Phys. A: Mater. Sci. Process. **63**, 207–216 (1996).
4. D. Braun and P. Fromherz, "Fluorescence interference-contrast microscopy of cell adhesion on oxidized silicon," Appl. Phys. A: Mater. Sci. Process. **65**, 341–348 (1997).
5. D. Braun and P. Fromherz, "Fluorescence interferometry of neuronal cell adhesion on microstructured silicon," Phys. Rev. Lett. **81**, 5241–5244 (1998).
6. J. M. Crane, V. Kiessling, and L. K. Tamm, "Measuring lipid asymmetry in planar supported bilayers by fluorescence interference contrast microscopy," Langmuir **21**, 1377–1388 (2005).
7. J. Kerssemakers, J. Howard, H. Hess, and S. Diez, "The distance that kinesin-1 holds its cargo from the microtubule surface measured by fluorescence interference contrast microscopy," Proc. Natl. Acad. Sci. U.S.A. **103**, 15812–15817 (2006).
8. A. K. Swan, L. Moiseev, C. R. Cantor, B. Davis, S. B. Ippolito, W. C. Karl, B. B. Goldberg, and M. S. Ünlü, "Towards nanometer-scale resolution in fluorescence microscopy using spectral self-interference," IEEE J. Sel. Top. Quantum Electron. **9**, 294–300 (2003).
9. L. Moiseev, M. S. Ünlü, A. K. Swan, B. B. Goldberg, and C. R. Cantor, "DNA conformation on surfaces measured by fluorescence self-interference," Proc. Natl. Acad. Sci. U.S.A. **103**, 2623–2628 (2006).
10. B. Davis, A. K. Swan, M. S. Ünlü, W. C. Karl, B. B. Goldberg, J. C. Schotland, and P. S. Carney, "Spectral self-interference microscopy for low signal nanoscale imaging," J. Opt. Soc. Am. A **24**, 3587–3599 (2007).
11. R. E. Colin, "Hertzian dipole radiating over a lossy earth or sea: Some early and late 20th-century controversies," IEEE Antennas Propag. Mag. **46**, 64–79 (2004).
12. N. Felsen and L. B. Marcuvitz, *Radiation and Scattering of Waves* (Wiley, 1994).
13. W. C. Chew, *Waves and Fields in Inhomogeneous Media*, series on Electromagnetic Waves (IEEE Press, 1995).
14. J. R. Mosig and F. E. Gardiol, "A dynamical radiation model for microstrip structures," in *Advances in Electronics and Electron Physics*, P. W. Hawkes, ed. (Academic, 1982), pp. 139–237.
15. K. A. Michalski and D. Zheng, "Electromagnetic scattering and radiation by surfaces of arbitrary shape in layered media: I. Theory," IEEE Trans. Antennas Propag. **38**, 335–344 (1990).
16. W. Lukosz and R. E. Kunz, "Light emission by magnetic and electric dipoles close to a plane interface I. Total radiated power," J. Opt. Soc. Am. **67**, 1607–1615 (1977).
17. W. Lukosz and R. E. Kunz, "Light emission by magnetic and electric dipoles close to a plane interface II. Radiation patterns of perpendicular oriented dipoles," J. Opt. Soc. Am. **67**, 1615–1619 (1977).
18. W. Lukosz, "Light emission by magnetic and electric dipoles close to a plane interface III. Radiation patterns of dipoles with arbitrary orientation," J. Opt. Soc. Am. **69**, 1495–1503 (1979).
19. W. Lukosz, "Theory of optical-environment-dependent spontaneous-emission rates for emitters in thin layers," Phys. Rev. B **22**, 3030–3038 (1980).
20. R. R. Chance, A. Prock, and R. Silbey, "Molecular fluorescence and energy transfer near interfaces," Adv. Chem. Phys. **37**, 1–65 (1978).
21. P. Török, "Propagation of electromagnetic dipole waves through dielectric interfaces," Opt. Lett. **25**, 1463–1465 (2000).
22. J. Enderlein and M. Böhmer, "Influence of interface–dipole interactions on the efficiency of fluorescence light collection near surfaces," Opt. Lett. **28**, 941–943 (2003).
23. M. I. Aksun and R. Mittra, "Derivation of closed-form Green's functions for a general microstrip geometry," IEEE Trans. Microwave Theory Tech. **MTT-40**, 2055–2062 (1992).
24. G. Dural and M. I. Aksun, "Closed-form Green's functions for general sources and stratified media," IEEE Trans. Microwave Theory Tech. **MTT-43**, 1545–1552 (1995).
25. M. I. Aksun, "A robust approach for the derivation of closed-form Green's functions," IEEE Trans. Microwave Theory Tech. **MTT-44**, 651–658 (1996).
26. M. I. Aksun and G. Dural, "Clarification of issues on the closed-form Green's functions in stratified media," IEEE Trans. Antennas Propag. **AP-53**, 3644–3653 (2005).
27. Y. Hua and T. K. Sarkar, "Generalized pencil-of-function method for extracting poles of an EM system from its transient response," IEEE Trans. Antennas Propag. **37**, 229–234 (1989).
28. J. Enderlein, "Theoretical study of detection of a dipole emitter through an objective with high numerical aperture," Opt. Lett. **25**, 634–636 (2000).
29. A. N. Vamivakas, S. B. Ippolito, A. K. Swan, M. S. Ünlü, M. Dogan, E. R. Behringer, and B. B. Goldberg, "Phase-sensitive detection of dipole radiation in a fiber-based high numerical aperture optical system," Opt. Lett. **32**, 970–972 (2007).
30. M. Dogan, A. Yalcin, S. Jain, M. B. Goldberg, A. K. Swan, M. S. Ünlü, and B. B. Goldberg, "Spectral self-interference fluorescence microscopy for subcellular Imaging" IEEE J. Sel. Top. Quantum Electron. **14**, 217–225 (2008).
31. L. A. Moiseev, C. R. Cantor, I. Aksun, M. Dogan, B. B. Goldberg, A. K. Swan, and M. S. Ünlü, "Spectral self-interference fluorescence microscopy," J. Appl. Phys. **96**, 5311–5315 (2004).
32. B. Levine, A. Kulik, and W. S. Bacsa, "Optical space and time coherence near surfaces," Phys. Rev. B **66**, 233404 (2002).

33. W. S. Bacsa and A. Kulik, "Interference scanning optical probe microscopy," Appl. Phys. Lett. **70**, 3507–3509 (1997).
34. B. Sick, B. Hecht, and L. Novotny, "Orientational imaging of single molecules by annular illumination," Phys. Rev. Lett. **85**, 4482–4485 (2000).
35. B. Davis and P. S. Carney, "Robust determination of the anisotropic polarizability of nanoparticles using coherent confocal microscopy," J. Opt. Soc. Am. A **25**, 2102–2113 (2008).
36. M. Böhmer and J. Enderlein, "Orientation imaging of single molecules by wide-field epifluorescence microscopy," J. Opt. Soc. Am. B **250**, 554–559 (2003).